Superwicking on Nanoporous Micropillared Surfaces

Deyin Zheng, Chang-Hwan Choi, Guangyi Sun, and Xin Zhao*

Read Online

ACCESS | Metrics & More | Article Recommendations | SI Supporting Information

ABSTRACT: Engineering surfaces with excellent wicking properties is of critical importance to a wide range of applications. Here, we report a facile method to create superhydrophilic nanoporous micropillared surfaces of silicon and their applicability to superwicking. Nanopores with a good control of the pore depth are realized over the entire surface of three-dimensional micropillar structures by electrochemical etching in hydrofluoric acid. After rinsing in hydrogen peroxide, the nanoporous micropillared surface shows superhydrophilicity with the superwicking effect. The entire spreading process of a water droplet on the superhydrophilic nanoporous micropillared surface is completed in less than 50 ms, with an average velocity of 91.2 mm/s, which is significantly faster than the other wicking surfaces reported. Owing to the presence of nanopores on the micropillar array, the wicking dynamics is distinct from the surfaces decorated only by micropillar arrays. The spreading dynamics of a water droplet shows two distinct processes simultaneously, including the capillary penetration between micropillars and the capillary imbibition into the nanopore's interior. The wicking dynamics can be described by the two stages separated by the time when the contact line starts to recede. The transition between the two wicking regimes is due to the increasing effect of the imbibition of the bulk droplet by the nanopores. While a similar transition of the wicking dynamics is shown on the surfaces with different pore depths, the nanopore structure with a greater depth causes a greater amount of imbibition to slow down the spreading and promote superwicking.

KEYWORDS: porous silicon, hierarchical structure, superhydrophilicity, spreading, hemi-wicking
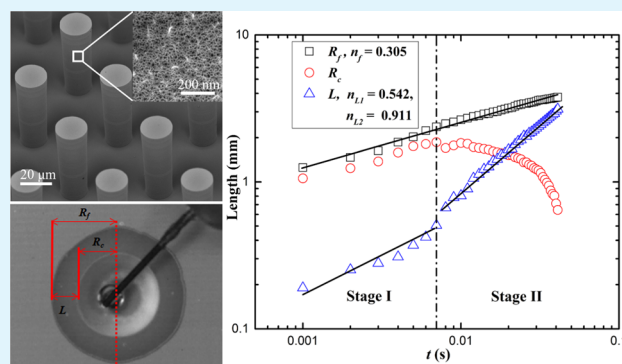
INTRODUCTION

Wicking is a dynamic wetting process during which a specific liquid penetrates into a porous system under the drive of capillary pressure. Through designing novel wicking structures with diverse materials, the efficiency of liquid transportation can be dramatically improved. In recent years, there is an increasing attention on developing advanced wicking structures because of their critical role in practical applications such as micro heat pipes,[1−3] nucleate boiling,[4−8] and water harvesting systems.[9] The wicking structures reported previously can be divided into three categories: microscale, nanoscale, and hierarchical structures. Liquid wicking on microstructured surfaces has been studied extensively, and the wicking length (L, relative distance between the liquid pool and wicking front) was found to follow a power law with respect to time (t) such as $L = k \cdot t^{0.5}$, where k can be derived by the balance between the capillary driving and viscous resistance.[10,11] A dense wicking structure possesses higher driving pressure, but it decreases the permeability because of viscous resistance. Therefore, specific wicking structures in practical applications are desirable based on the trade-off between these two competing considerations. In using nanostructured surfaces, the wetting and wicking performance can also be improved because of the relatively large surface roughness and capillary pressure. Liquid spreading on surfaces with different kinds of nanoscale roughness such as nanowires and nanopillars has been investigated both experimentally and theoretically. On nanostructured surfaces, the wicking length was also found to obey similar dynamic behaviors as on microstructured surfaces.[5,12−14] Although the nanoscale roughness can increase the capillary driving pressure, the liquid flow will also be compromised by the relatively low permeability or large viscous dissipation. Therefore, liquid transportation on nanostructured surfaces still experiences a relatively slow spreading velocity, which is undesirable in practical applications.
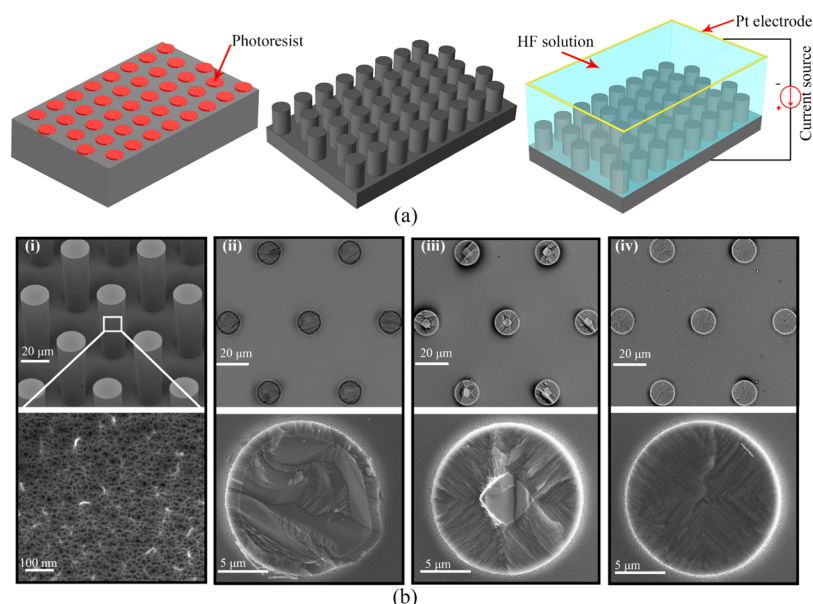
More recently, hierarchical structures with dual-scaled roughness have been demonstrated to have outstanding wicking speed compared to single-scaled structures.[2,15−18] Comparing with the single-scaled structures, the wicking speed for a liquid on hierarchical structures was enhanced significantly. For hierarchically structured surfaces, the power
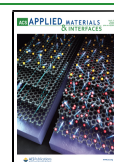
Figure 1. (a) Schematic illustration of the process flow for fabrication of nanoporous micropillared surfaces. (b) SEM images of the nanoporous micropillared surfaces. The view in (i) was acquired at an angle of 45°. (ii−iv) Represent the cross-sectional top-view of the details inside the nanoporous micropillars with increasing pore depths, corresponding to the samples prepared by an etching time of 10, 30, and 50 min, respectively. The images below (ii−iv) correspond to the close-up views of the nanoporous micropillars.

law $L = k \cdot t^{0.5}$ has also been found to be valid for the wicking length versus time but with a greater value for the pre-exponential constant k. However, the secondary roughness is not always found to be beneficial to liquid wicking, especially as the primary structures are on the order of submicron.[15,18] In such a case, although the wetting ability can be improved by adding the secondary roughness, the wicking channels are also narrowed down by the presence of the secondary roughness. As a result, an additional viscous loss associated with the secondary roughness may be introduced. To date, most superfast wicking phenomena have been realized on hierarchical structures of metallic substrates composing of micrometer-scale primary structures and nanoscale secondary roughness.[2,16−18] Recently, the development of advanced silicon-based thermal management technology has brought forward greater requirement of optimized wicking structures for silicon substrates.[19,20] In this study, nanopores rather than nanowires are tested as the second level of roughness to the microstructured surface of silicon. We expect that nanopores, as opposed to nanowires, will not narrow the liquid channels so that a droplet may not experience the significant viscous loss associated with the additional roughness. Nanopores have disconnected internal spaces which are distinct from the nanowires or nanopillars conventionally employed in hierarchical structures. Despite little viscous loss, the nanopores will introduce the effect of liquid imbibition.[21−23] Currently, however, the effects of nanopores on the wicking dynamics in the hierarchical structures have not been systematically understood yet. In this study, we report a systematic experimental test on droplet spreading and wicking dynamics, using the micropillared surfaces of silicon which are further hierarchically patterned with nanopores.

■ EXPERIMENTAL SECTION

Surface Preparation. The fabrication process of nanoporous micropillared surfaces is illustrated in Figure 1a. A highly doped P-type (100) Si wafer was first cleaned and spin-coated with a thin

photoresist layer (AZ 6130, MicroChemicals) of ∼3 μm thickness. Then, photolithography was performed by exposing the coated photoresist under UV (ultra-violet) light using a mask aligner (MA6, Karl Suss, Germany). The exposed photoresist was then removed using the developing solution (RZX-3038, Suzhou Ruihong CO., Ltd.), followed by baking at 110 °C for 2.5 min. The silicon deep reactive ion etching process was performed with an inductively coupled plasma etching machine (Surface Technologies Systems USA Inc., Redwood, CA). The etched wafer was then cleaned thoroughly and cleaved into 2 cm × 2 cm square pieces with 1.5 cm × 1.5 cm effective micropillared area. Nanopore patterns were then created on the micropillared surface by applying electrochemical etching. Before this process, the gallium/indium (Ga/In) eutectic was uniformly applied on the backside of the small chip to ensure homogeneous current distribution during etching. A platinum plate with the same size to the sample was used to serve as the cathode. Then, the micropillared surface was decorated with nanopores by applying electrochemical etching in hydrofluoric (HF) solution (10 wt % HF in deionized water at 20 °C) under anodic bias conditions with a constant current density (10 mA/cm²).

Figure 1b shows the distribution and internal details of the nanoporous micropillar arrays. Field-emission scanning electron microscopy (SU 8010, Hitachi) was used to examine the surface morphology of the samples. The measurement of pore diameters and pore depths was estimated by processing the SEM images in ImageJ software. The micropillar arrays have a hexagonal distribution with a diameter of 20 μm, pitch of 50 μm, and height of 50 μm. A hierarchical structure is achieved after the decoration of nanopores, consisting of a microscale pillar structure additionally featured with nanoporous structures (pore diameters less than 50 nm). The pore dimensions were estimated by processing the magnified SEM images using ImageJ software. The pores grow perpendicular to the micropillar surfaces, and the depths can be conveniently manipulated by varying the etching times. The nanoporous micropillared surfaces etched for 10, 30, and 50 min have pore depths of 1.5, 5.1, and 7.6 μm, respectively.

Surface Modification. After the electrochemical etching process, the samples were rinsed in ethanol and then were dried with compressed air. In order to make the surface hydrophilic, the as-prepared samples were soaked in hydrogen peroxide solution (30 wt %) with an addition of 5% ethanol at the temperature of 4 °C for 4 h.

The addition of ethanol into the hydrogen peroxide solution facilitates the penetration of the solution into the interior of the porous surfaces. After the treatment, the samples were rinsed by deionized water, followed by being dried on a hot plate at a temperature of 100 °C for 2 min. Kumar et al. reported that the average pore diameter was reduced by a limited amount of ~1/3 after treatment by H_2O_2 for 10 h.[24] In this study, a shorter treatment time (4 h) was applied so that the reduction of the pore diameter was not significant. Nonetheless, the average diameter of our samples should still be less than 50 nm, falling into a mesopore regime.

Characterizations of Wetting and Spreading Properties. Contact angles of droplets on surfaces were measured by using a home-made contact angle meter at room conditions (25 °C, atmospheric pressure, RH = 50%). The captured images were processed using DropSnake Plugin for ImageJ software. The contact angles were measured at three different locations of each samples. The values of the contact angles reported are the mean and standard deviation. As for the measurement of droplet spreading on the nanoporous micropillared surfaces, a high-precision microsyringe pump system was used to generate microdroplets (Figure 2). A high-
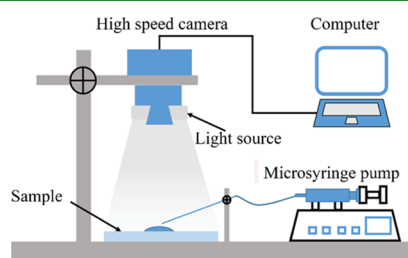

Figure 2. Experimental setup for characterization of droplet spreading.

speed camera (Photron UX 50) was used to capture the dynamics with a resolution of 1280 × 1024 at a recording speed of 1000 fps. The sample was mounted horizontally on the stage. To minimize the gravity and inertial effect when applying droplets onto the samples, the syringe tip was placed at a distance of ~2 mm (less than the capillary length of water, ~2.73 mm) above the sample. During the injection, the droplet collapses and spreads on the surface simultaneously when the diameter of a water droplet increases to ~2 mm and contacts with the surface.

■ RESULTS AND DISCUSSION

Wetting Property of Nanoporous Micropillared Surfaces. Because the wettability is determined by surface roughness and chemistry, hierarchical structures that can provide multiscale roughness have been used to promote hydrophobicity as well as hydrophilicity of surfaces.[25,26] As shown in Figure 3, the as-prepared nanoporous micropillar arrays initially showed hydrophobicity with an apparent contact angle of ~146° with low contact angle hysteresis, regardless of the pore depths (see Table S1 in Supporting Information). For comparison, the contact angle on a flat silicon substrate and a micropillared silicon, which was soaked in a HF solution (10 wt %), was also measured. Soaking in HF solution was to remove the oxide layer on the surface, making the surface hydrogen-terminated, exhibiting hydrophobicity.[27−30] As shown in Figure 3, the apparent contact angle on the HF-treated flat silicon substrate is approximately 89°. It increases to approximately 145° on the HF-treated micropillared substrate. Theoretically, the transition or critical contact angle of a flat surface to determine between the Cassie−Baxter and Wenzel state is 90°.[11,31] However, in practice, an advancing contact angle rather than the theoretical
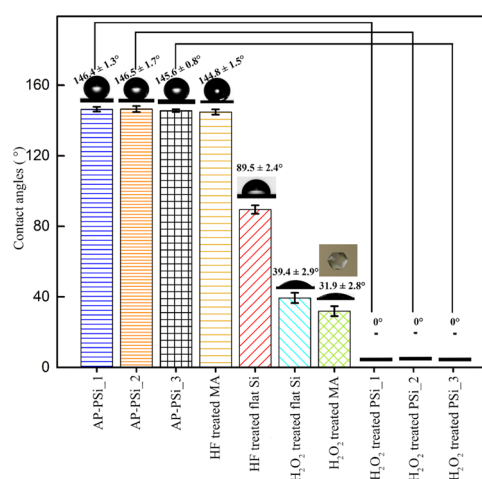
Figure 3. Apparent contact angles of water droplets on different samples. From left to right: as-prepared (AP), nanoporous micropillared silicon (PSi) surfaces with increasing pore depths (corresponding to Figure 1b), HF-treated micropillar array (MA), HF-treated flat silicon, H_2O_2-treated flat silicon, H_2O_2-treated micropillar array, and H_2O_2-treated nanoporous micropillared silicon surfaces with increasing pore depths.

equilibrium contact angle determines the transition. Previous studies showed that the surfaces with an as-deposited contact angle of less than 90° (usually between 70 and 80°) could provide the Cassie−Baxter state with roughness.[32,33] The as-deposited contact angle of the HF-treated flat surface was 89°, which is much greater than the typical critical angle reported (70−80°), suggesting that the advancing contact angle should be much more than 90°. Thus, the HF-treated microstructured surface exhibits the Cassie−Baxter state. For the nanoporous micropillar arrays, the secondary nanoporous structures grow inward instead of outward from the micropillar surface. Therefore, the nanoporous micropillar array is a kind of a recessive hierarchical structure which is distinct from the typical protruding hierarchical structures using nanopillars or nanowires as secondary structures. While protruding nano-structures usually provide additional sites for trapping the air layer and hence promote the hydrophobicity (e.g., increase in contact angle), the result shows that the recessive nanopore structures do not significantly enhance the hydrophobicity becausee of the recessive nature of the porous surface topography.

Surface Hydrophilization. In contrast to the hydrophobic nature of the HF-treated silicon surface, the silicon surface treated by soaking in hydrogen peroxide (H_2O_2) exhibits hydrophilicity. Soaking in H_2O_2 solution makes the surface hydrophilic because of the presence of silanol groups (Si−OH).[27−30] In a hydrophilic regime, the hydrodynamics of the droplet deposited on a rough surface depends significantly on the intrinsic wettability and surface morphology. The intrinsic wettability (i.e., equilibrium contact angle θ_e) and surface morphology determine an apparent contact angle θ^* and a critical angle θ_c. The critical angle θ_c can be expressed as follows[11]

$$\theta_c = \cos^{-1}((1 - \varphi)/(r - \varphi)) \tag{1}$$

where r is the surface roughness, and φ is the top area fraction of the liquid−solid interface (so-called solid fraction). When θ_c
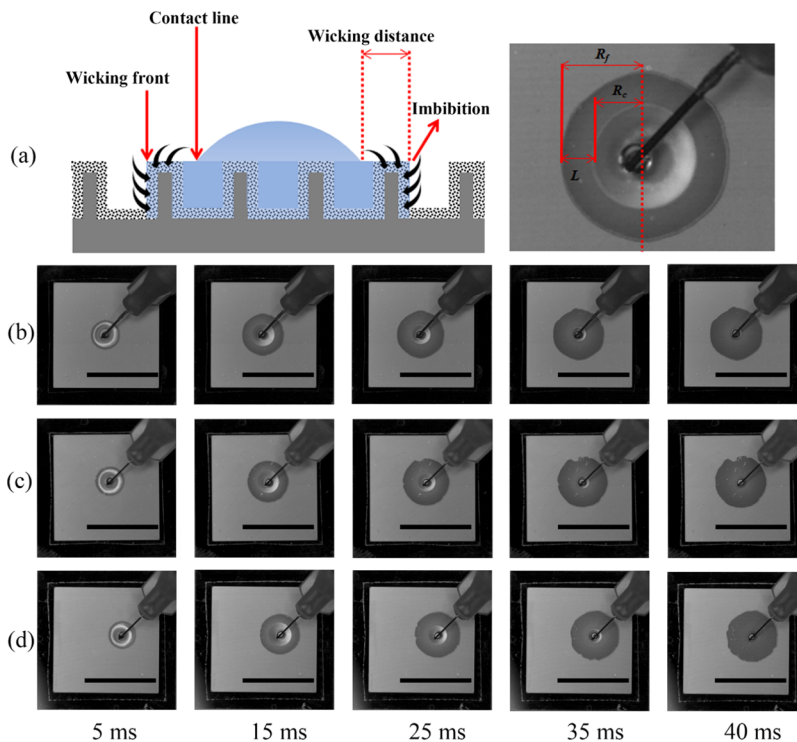
Figure 4. Water droplet wicking on the nanoporous micropillared surfaces. (a) Illustration of droplet wicking on nanoporous micropillared surfaces. (b−d) Snapshots of water droplet wicking on nanoporous micropillared substrates with increasing pore depths of 1.5, 5.1, and 7.6 μm, respectively. The scale bar in each image represents 10 mm. Videos are attached in the Supporting Information.
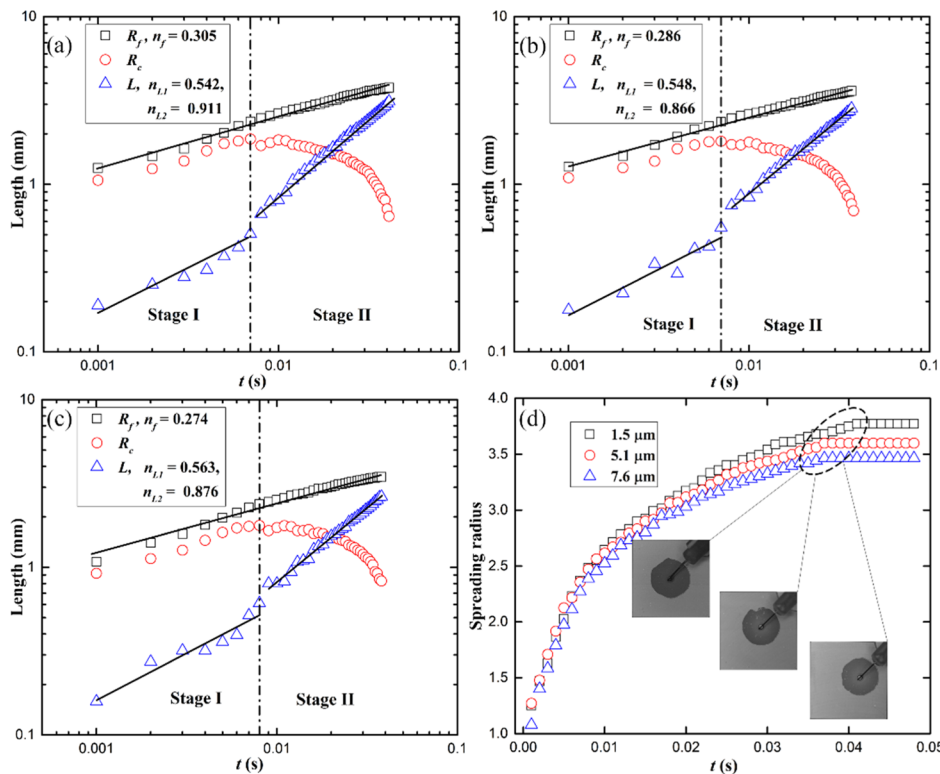
Figure 5. Spreading and wicking dynamics of water droplets on the nanoporous micropillared silicon surface with different pore depths. (a) Pore depth of 1.5 μm. (b) Pore depth of 5.1 μm. (c) Pore depth of 7.6 μm. (d) Spreading curves of droplets on nanoporous micropillared surfaces with different pore depths. From left to right, the insets show the final spreading areas on the nanoporous micropillared surfaces with increasing pore depths.

$< \theta_e < 90°$, the hydrophilicity is enhanced with a reduced contact angle θ^* predicted by Wenzel's model.[11,31]

$$\cos \theta^* = r \cdot \cos \theta_e \tag{2}$$

On the other hand, when $\theta_e < \theta_c$, hemi-wicking will occur. In this case, the droplet will penetrate spontaneously into the roughness, and the droplet will eventually sit on a hybrid surface composed of water and silicon. The main difference between the Wenzel state and hemi-wicking is that in a Wenzel state the structured surface is wetted only immediately adjacent to the liquid drop, whereas in hemi-wicking the surface is wetted in an area beyond the extent of the drop. The corresponding contact angle of the equilibrium state in hemi-wicking can be expressed as follows[11]

$$\cos \theta^* = 1 - \varphi \cdot (1 - \cos \theta_e) \quad (3)$$

For the micropillared surface, the critical contact angle, surface roughness, and solid fraction are 68°, 2.45, and 0.14, respectively. Meanwhile, the apparent contact angle on the flat substrate is ~39°, which can approximate the equilibrium contact angle θ_e. Thus, the hydrodynamics on the micropillared surface should fall into hemi-wicking. However, the apparent contact angle measured on the micropillared substrate was ~32°, which is much higher than the predicted value of 14° by eq 3. This is due to the significant pinning of the contact line by the micropillar structures. Thus, the droplet does not spread out completely (i.e., does not show hemi-wicking), and its base takes the orthohexagonal shape, which conforms to the hexagonal distribution of micropillars. As opposed to the micropillared surface, the nanoporous micropillared surfaces with a rinse in H_2O_2 displayed extreme superhydrophilicity with an apparent contact angle of 0°, regardless of the pore depths. This result indicates that the created nanoporous layer combined with proper surface modification could enable superhydrophilicity of the micropillared surfaces, guaranteeing hemi-wicking.

Superwicking Properties. Figure 4 shows the spreading and wicking behaviors of water droplets measured on the H_2O_2-treated nanoporous micropillared silicon surfaces. We analyze the kinetics of the wicking process for the radius of the wicking front (R_f), the radius of contact line (R_c), and the wicking distance ($L = R_f - R_c$), as illustrated in Figure 4a. Figure 4b−d shows images taken from the droplet spreading video with increasing time. Because of the superhydrophilic nature of the substrates, the droplets collapse instantly upon touching the surfaces. The superhydrophilic nature of the nanoporous micropillars (i.e., capillarity) facilitates the super-fast spreading of droplets on the surface. The spreading areas increase rapidly and display a rounded hexagonal shape. The droplet on the micropillared surface can be divided into two parts: the fringe layer formed by the wicking of water and the remaining bulk droplet. During the spreading, the fringe is driven by the capillary pressure provided by the space between the micropillars, and the bulk droplet acts as the reservoir to supply the expansion of the fringe.

To investigate the effects of the nanoporous layer on the spreading dynamics, we measured the spreading distances (R_f), droplet radii (R_c), and wicking distances (L) with respect to time on the nanoporous micropillared surfaces with different pore depths, as shown in Figure 5. During the evolution of the droplet spreading, the contact line and wicking front were found proceeding separately from the beginning. In the early stage, the wicking front propagates ahead of the contact line, both of which increase monotonously with time. Then, the contact line starts to recede gradually until the droplet is exhausted. It can be found clearly that evolution of R_f follows a power-law behavior $R_f \propto t^n$ for the entire spreading process.

Specifically, the power-law fitting of R_f on the nanoporous micropillared surfaces with the different pore depths gives the exponent values of $n_f = 0.305$, 0.286, and 0.274 for the pore depths of 1.5, 5.1, and 7.6 μm, respectively. While the nanopore structure with a greater depth slows down the spreading, which is attributed to the greater amount of imbibition of water into the pore structures, the values of n_f fall in the range of spreading on pillar-arrayed surfaces, on which the exponent n_f ranged from 0.108 to 0.33 in the literature.[34−36]

For the wicking length L, we divided the process into two stages separated by the time when the contact line starts to recede. In stage I, the power-law fitting gives $n_{L1} = 0.542$, 0.548, and 0.563 for the pore depths of 1.5, 5.1, and 7.6 μm, respectively. The kinetics generally follows the power-law relation $L \propto t^{1/2}$, which is consistent with the droplet wicking shown on traditional hierarchical structures.[16−18] In stage II, the slope of the fitting curve increases to $n_{L2} = 0.911$, 0.866, and 0.876 for the pore depths of 1.5, 5.1, and 7.6 μm, respectively. The increase in the value of n_L from stage I to stage II indicates the more significant effect of the nanoporous layer on the spreading behavior in stage II. The transition of wicking dynamics can be interpreted in a manner of surface energy analysis. Because the drop size (4 μL, ~1 mm in radius) is less than the capillary length (~2.7 mm for water), the inertial effect such as gravity can be neglected. When the droplet comes into contact with a surface, the surface energy is lowered by being wet by water. The energy change associated with the wicking length L can be expressed as

$$dE = \pi \cdot [\gamma + r \cdot (\gamma_{SL} - \gamma_{SG}) + r' \cdot (\gamma_{SL} - \gamma_{SG})] \cdot d(R_f{}^2 - R_c{}^2) \quad (4)$$

where γ, γ_{SL}, and γ_{SG} are interfacial tensions between liquid and air, solid and liquid, and solid and air, respectively, and r' is the surface roughness introduced by nanopores.[34] The driving capillary force can be calculated by $F_c = -dE/dL$. For stage I, the wicking distance L is relatively small and $R_c = R_f - L$. Then, the capillary force in stage I can be reduced to be

$$F_{c1} = 2\pi \cdot R_f \cdot \gamma \cdot [(r + r') \cdot \cos \theta_e - 1] \quad (5)$$

For stage II, the wicking distance L cannot be neglected. Then, the capillary force in stage II can be reduced to be

$$F_{c2} = 2\pi \cdot \gamma \cdot [(r + r') \cdot \cos \theta_e - 1] \cdot (R_f - L) \quad (6)$$

Meanwhile, the viscous resistance scales as

$$F_r \sim \pi \cdot (R_f{}^2 - R_c{}^2) \cdot \mu \cdot r \cdot \dot{L}/h \sim \pi \cdot (2R_f - L) \cdot L \cdot \mu \cdot r \cdot \dot{L}/h \quad (7)$$

where μ is the dynamic viscosity of the liquid, and h is the pillar height.[34] Balancing the driving capillary force and the viscous resistance leads to two distinct wicking dynamics for the two different stages. For stage I, by balancing eqs 5 and 7, the wicking distance can be characterized as

$$L \sim \sqrt{\frac{h \cdot \gamma \cdot [(r + r') \cdot \cos \theta_e - 1]}{\mu \cdot r}} \cdot t^{1/2} \quad (8)$$

This prediction agrees well with the fitting exponents (n_{L1}) for the correlation between the wicking distance (L) and time (t) obtained in the experiments. Equation 8 also suggests that the secondary roughness (r') should facilitate the wicking speed. Although the difference in the fitting exponents with respect to the pore depth is not prominent, the apparently

increasing trend of the fitting exponents n_{L1} from 0.542 to 0.548 to 0.563 for the pore depths from 1.5 to 5.1 to 7.6 μm supports the theoretical model. For stage II, balancing eqs 6 and 7, we obtain

$$\frac{dL}{dt} = \frac{M \cdot (R_f - L)}{(2R_f - L) \cdot L} \tag{9}$$

where $M = N \cdot h \cdot \gamma \cdot [(r + r') \cdot \cos \theta_e - 1]/(\mu \cdot r)$ is the coefficient determined by the physical parameters of the liquid (i.e., water) and the geometrical parameters of surface roughness, and N is a scaling factor. Although eq 9 cannot be analytically solved, eq 9 shows that the wicking dynamics in stage II is distinctive from that in stage I. It also suggests that the effect of a pore depth (i.e., r' in M) on L should be more significant in stage II, supporting the experimental results shown in Figure 5.

Because of the highly porous nature, the porous layer acts as an absorber and sucks water. Because of the secondary effects of the nanopore structures for water to fill, in addition to the improved wetting behavior by micropillars for wicking, the entire spreading of a water droplet on the nanoporous micropillared surface completed within less than 50 ms with an average spreading velocity of 91.2 mm/s, which is significantly faster than that of a droplet having the similar volume (1−5 μL) on the other wicking surfaces reported so far (see Table S2 in Supporting Information).[36−39] During stage I, the absorbed volume of water is insignificant compared with that of the bulk droplet. With the increase in the spreading area, a considerable amount of volume is sucked to fill the pores of the nanoporous layer. Thus, the effect of the additional nanoporous layer in the micropillar structures starts to become crucial in stage II, compared to stage I. The estimated time scales of the imbibition process by nanopores are on the order of 0.01−0.1 ms (see Supporting Information). The entire spreading time of the droplet is in the order of 10 ms, which is about 2−3 orders of magnitude greater than the filling time of the nanopores. This indicates that the time scale of the nanopore imbibition is much faster than that of the micropillars, implying that the effect of water imbibition to the secondary nanopores should trigger the distinctive transition of the wicking and spreading dynamics across the micropillars in a timely manner. The significance of the imbibition of water can also be verified by the comparison of the spreading distance (R_f) on the nanoporous micropillar surfaces with different pore depths, as shown in Figure 5d. It shows a clear trend that the greater the pore depth, the more the absorbed volume of water and hence the smaller the spreading area and spreading velocity.

CONCLUSIONS

In this work, we have studied the spreading and wicking dynamics of nanoporous micropillared surfaces systematically. Wetting transition from original hydrophobicity to super-hydrophilicity was realized by the modification of surface chemistry as well as the addition of the secondary nanopore structures to the initial micropillar structures. The secondary nanopore structures allowed the micropillared surface to show the superwicking effect. Water droplets on the nanoporous micropillared surfaces show distinct wicking dynamics resulting from the joint effects of capillary driving by the micropillars and the imbibition of liquids into the nanopore's interior. The nanopore structure with a greater depth causes a greater amount of imbibition so that it slows down the spreading.

Nonetheless, the spreading velocities on the nanoporous micropillared surface are still significantly faster than the other hierarchical wicking structures reported so far. Although this method cannot be easily expanded to a wide spectrum of materials, we envision that this hierarchical silicon structure can be integrated flexibly into the silicon-based thermal management devices. The distinct surface roughness can help prevent dry-out and facilitate the reflow of coolants. Considering such advantages and unique effects of a secondary nanoporous layer on the spreading and wicking behaviors, the demonstrated approach will be of great significance in the applications of silicon-based heat pipes and microchannel heat sinks. In addition, the proposed nanoporous micropillared surfaces will serve as a feasible candidate for the advanced intrachip level cooling technology.

ASSOCIATED CONTENT

Supporting Information

The Supporting Information is available free of charge at https://pubs.acs.org/doi/10.1021/acsami.0c04366.

> Advancing and receding contact angles of the untreated nanoporous micropillared surfaces; comparison of the spreading time and average spreading velocity of a water droplet between this and other prior studies; and water imbibition analysis inside the nanopores (PDF)
>
> Droplet spreading on nanoporous micropillared surfaces with a pore depth of 1.5 μm (MPG)
>
> Droplet spreading on nanoporous micropillared surfaces with a pore depth of 5.1 μm (MPG)
>
> Droplet spreading on nanoporous micropillared surfaces with a pore depth of 7.6 μm (MPG)

AUTHOR INFORMATION

Corresponding Author

Xin Zhao − *Institute of Robotics and Automatic Information System, Nankai University, Tianjin 300071, P. R. China;* Email: zhaoxin@nankai.edu.cn

Authors

Deyin Zheng − *Institute of Robotics and Automatic Information System, Nankai University, Tianjin 300071, P. R. China;* orcid.org/0000-0001-5345-5744

Chang-Hwan Choi − *Department of Mechanical Engineering, Stevens Institute of Technology, Hoboken, New Jersey 07030, United States;* orcid.org/0000-0003-2715-7393

Guangyi Sun − *Institute of Robotics and Automatic Information System, Nankai University, Tianjin 300071, P. R. China;* orcid.org/0000-0003-1362-750X

Complete contact information is available at:
https://pubs.acs.org/10.1021/acsami.0c04366

Notes

The authors declare no competing financial interest.

ACKNOWLEDGMENTS

■ REFERENCES

(1) Sigurdson, M.; Liu, Y.; Bozorgi, P.; Bothman, D.; MacDonald, N.; Meinhart, C. A Large Scale Titanium Thermal Ground Plane. *Int. J. Heat Mass Transfer* **2013**, *62*, 178−183.

(2) Nam, Y.; Sharratt, S.; Byon, C.; Kim, S. J.; Ju, Y. S. Fabrication and Characterization of the Capillary Performance of Super-hydrophilic Cu Micropost Arrays. *J. Microelectromech. Syst.* **2010**, *19*, 581−588.

(3) Ding, C.; Soni, G.; Bozorgi, P.; Piorek, B. D.; Meinhart, C. D.; Macdonald, N. C. A Flat Heat Pipe Architecture Based on Nanostructured Titania. *J. Microelectromech. Syst.* **2010**, *19*, 878−884.

(4) Chen, R.; Lu, M.-C.; Srinivasan, V.; Wang, Z.; Cho, H. H.; Majumdar, A. Nanowires for Enhanced Boiling Heat Transfer. *Nano Lett.* **2009**, *9*, 548−553.

(5) Shim, D. I.; Choi, G.; Lee, N.; Kim, T.; Kim, B. S.; Cho, H. H. Enhancement of Pool Boiling Heat Transfer using Aligned Silicon Nanowire Arrays. *ACS Appl. Mater. Interfaces* **2017**, *9*, 17595−17602.

(6) Kim, D. E.; Park, S. C.; Yu, D. I.; Kim, M. H.; Ahn, H. S. Enhanced Critical Heat Flux by Capillary Driven Liquid Flow on the Well-designed Surface. *Appl. Phys. Lett.* **2015**, *107*, 023903.

(7) Shin, S.; Choi, G.; Rallabandi, B.; Lee, D.; Shim, D. I.; Kim, B. S.; Kim, K. M.; Cho, H. H. Enhanced Boiling Heat Transfer using Self-Actuated Nanobimorphs. *Nano Lett.* **2018**, *18*, 6392−6396.

(8) Dhillon, N. S.; Buongiorno, J.; Varanasi, K. K. Critical Heat Flux Maxima During Boiling Crisis on Textured Surfaces. *Nat. Commun.* **2015**, *6*, 8247.

(9) Dai, X.; Sun, N.; Nielsen, S. O.; Stogin, B. B.; Wang, J.; Yang, S.; Wong, T. S. Hydrophilic Directional Slippery Rough Surfaces for Water Harvesting. *Sci. Adv.* **2018**, *4*, No. eaaq0919.

(10) Courbin, L.; Denieul, E.; Dressaire, E.; Roper, M.; Ajdari, A.; Stone, H. A. Imbibition by Polygonal Spreading on Microdecorated Surfaces. *Nat. Mater.* **2007**, *6*, 661−664.

(11) Quéré, D. Wetting and Roughness. *Annu. Rev. Mater. Res.* **2008**, *38*, 71−99.

(12) Chen, X.; Chen, J.; Ouyang, X.; Song, Y.; Xu, R.; Jiang, P. Water Droplet Spreading and Wicking on Nanostructured Surfaces. *Langmuir* **2017**, *33*, 6701−6707.

(13) Mai, T. T.; Lai, C. Q.; Zheng, H.; Balasubramanian, K.; Leong, K. C.; Lee, P. S.; Lee, C.; Choi, W. K. Dynamics of Wicking in Silicon Nanopillars Fabricated with Interference Lithography and Metal-assisted Chemical Etching. *Langmuir* **2012**, *28*, 11465−11471.

(14) Kim, B. S.; Lee, H.; Shin, S.; Choi, G.; Cho, H. H. Interfacial Wicking Dynamics and Its Impact on Critical Heat Flux of Boiling Heat Transfer. *Appl. Phys. Lett.* **2014**, *105*, 191601.

(15) Charlton, J. J.; Lavrik, N.; Bradshaw, J. A.; Sepaniak, M. J. Wicking Nanopillar Arrays with Dual Roughness for Selective Transport and Fluorescence Measurements. *ACS Appl. Mater. Interfaces* **2014**, *6*, 17894−17901.

(16) Lee, J.; Suh, Y.; Dubey, P. P.; Barako, M. T.; Won, Y. Capillary Wicking in Hierarchically Textured Copper Nanowire Arrays. *ACS Appl. Mater. Interfaces* **2018**, *11*, 1546−1554.

(17) Zuruzi, A. S.; Gardner, H. C.; Monkowski, A. J.; MacDonald, N. C. Tailored Nanostructured Titania Integrated on Titanium Micro-pillars with Outstanding Wicking Properties. *Lab Chip* **2013**, *13*, 2414−2418.

(18) Wang, Z.; Zhao, J.; Bagal, A.; Dandley, E. C.; Oldham, C. J.; Fang, T.; Parsons, G. N.; Chang, C.-H. Wicking Enhancement in Three-dimensional Hierarchical Nanostructures. *Langmuir* **2016**, *32*, 8029−8033.

(19) Sarvey, T. E.; Hu, Y.; Green, C. E.; Kottke, P. A.; Woodrum, D. C.; Joshi, Y. K.; Fedorov, A. G.; Sitaraman, S. K.; Bakir, M. S. Integrated Circuit Cooling Using Heterogeneous Micropin-Fin Arrays for Nonuniform Power Maps. *IEEE Trans. Compon., Packag., Manuf. Technol.* **2017**, *7*, 1465−1475.

(20) Sarvey, T. E.; Zhang, Y.; Cheung, C.; Gutala, R.; Rahman, A.; Dasu, A.; Bakir, M. S. Monolithic Integration of a Micropin-Fin Heat Sink in a 28-nm FPGA. *IEEE Trans. Compon., Packag., Manuf. Technol.* **2017**, *7*, 1617−1624.

(21) Haidara, H.; Lebeau, B.; Grzelakowski, C.; Vonna, L.; Biguenet, F.; Vidal, L. Competitive Spreading versus Imbibition of Polymer Liquid Drops in Nanoporous Membranes: Scaling Behavior with Viscosity. *Langmuir* **2008**, *24*, 4209−4214.

(22) Clarke, A.; Blake, T. D.; Carruthers, K.; Woodward, A. Spreading and Imbibition of Liquid Droplets on Porous Surfaces. *Langmuir* **2002**, *18*, 2980−2984.

(23) Zadražil, A.; Stepanek, F.; Matar, O. Droplet Spreading, Imbibition and Solidification on Porous Media. *J. Fluid Mech.* **2006**, *562*, 1−33.

(24) Kumar, P.; Hofmann, T.; Knorr, K.; Huber, P.; Scheib, P.; Lemmens, P. Tuning the pore wall morphology of mesoporous silicon from branchy to smooth, tubular by chemical treatment. *J. Appl. Phys.* **2008**, *103*, 024303.

(25) Kim, B. S.; Shin, S.; Shin, S. J.; Kim, K. M.; Cho, H. H. Micro-nano Hybrid Structures with Manipulated Wettability using a Two-step Silicon Etching on a Large Area. *Nanoscale Res. Lett.* **2011**, *6*, 333.

(26) Guo, Z.; Liu, W.; Su, B.-L. Superhydrophobic Surfaces: from Natural to Biomimetic to Functional. *J. Colloid Interface Sci.* **2011**, *353*, 335−355.

(27) Lehmann, V. *Electrochemistry of Silicon: Instrumentation, Science, Materials and Applications*; Wiley, 2002.

(28) Ulin, V. P.; Ulin, N. V.; Soldatenkov, F. Y.; Semenov, A. V.; Bobyl, A. V. Surface of Porous Silicon under Hydrophilization and Hydrolytic Degradation. *Semicond* **2014**, *48*, 1211−1216.

(29) Guhathakurta, S.; Subramanian, A. Effect of Hydrofluoric Acid in Oxidizing Acid Mixtures on the Hydroxylation of Silicon Surface. *J. Electrochem. Soc.* **2007**, *154*, P136−P146.

(30) Muñoz, E. C.; Díaz, C.; Navarrete, E.; Henríquez, R.; Schrebler, R.; Córdova, R.; Heyser, C. Characterization of Surface Changes on Silicon and Porous Silicon after Interaction with Hydroxyl Radicals. *Arab. J. Chem.* **2019**, *12*, 5125−5133.

(31) Wenzel, R. N. Resistance of Solid Surfaces to Wetting by Water. *Ind. Eng. Chem.* **1936**, *28*, 988−994.

(32) Dattilo, D.; Armelao, L.; Maggini, M.; Fois, G.; Mistura, G. Wetting Behavior of Porous Silicon Surfaces Functionalized with a Fulleropyrrolidine. *Langmuir* **2006**, *22*, 8764−8769.

(33) Palasantzas, G.; de Hosson, J. T. M. Wetting on Rough Surfaces. *Acta Mater.* **2001**, *49*, 3533.

(34) Kim, S. J.; Moon, M.-W.; Lee, K.-R.; Lee, D.-Y.; Chang, Y. S.; Kim, H.-Y. Liquid Spreading on Superhydrophilic Micropillar Arrays. *J. Fluid Mech.* **2011**, *680*, 477−487.

(35) Zong, D.; Yang, Z.; Duan, Y. Dynamic Spreading of Droplets on Lyophilic Micropillar-arrayed Surfaces. *Langmuir* **2018**, *34*, 4417−4425.

(36) Fan, J.-G.; Zhao, Y.-P. Spreading of a Water Droplet on a Vertically Aligned Si Nanorod Array Surface. *Appl. Phys. Lett.* **2007**, *90*, 013102.

(37) Lai, C. Q.; Mai, T. T.; Zheng, H.; Lee, P. S.; Leong, K. C.; Lee, C.; Choi, W. K. Droplet spreading on a Two Dimensional Wicking Surface. *Phys. Rev. E: Stat., Nonlinear, Soft Matter Phys.* **2013**, *88*, 062406.

(38) Ahn, H. S.; Park, G.; Kim, J.; Kim, M. H. Wicking and Spreading of Water Droplets on Nanotubes. *Langmuir* **2012**, *28*, 2614−2619.

(39) Vorobyev, A. Y.; Guo, C. Laser Turns Silicon Superwicking. *Opt. Express* **2010**, *18*, 6455−6460.